CHEMISTRY

Multi-component gradients in 3D host frameworks enabled stack-type zinc plating/stripping for highly durable aqueous Zn-ion batteries

Jingjie Sun[1], Tianyu Shen[1,2], Mingyue Zhang[3], Yizhi Xing[1], Jie Wei[1], Qianchuan Yu[1], Zuoxiu Tie[1], Zhong Jin[1]*

Developing dendrite-free zinc metal anodes with high durability poses a great challenge for aqueous zinc-ion batteries. Herein, we propose an in situ constructed 3D restrained host frameworks with multi-component gradients that induces a controllable and rapid stack-type zinc plating/stripping behavior, enabling a unique "first-in/last-out" mode. Typically, hydrophobic amino-functionalized polysilane passivation layer and zincophilic Ag nanoparticles are successively self-assembled on carbon paper scaffold to form opposite concentration gradients, namely *g'*-Ag/*g*-PSiO_x-NH_2/CP. The *g*-PSiO_x-NH_2 inhibits side-reactions and promotes Zn^{2+} desolvation, meanwhile the *g'*-Ag guides preferential Zn^{2+} deposition. Consequently, the zinc-deposited *g'*-Ag/*g*-PSiO_x-NH_2/CP electrodes exhibit high Coulombic efficiency and long cyclability, surpassing 5000 hours at 10 mA cm^{-2}/10 mAh cm^{-2} in symmetric cells. The as-assembled Zn||MnO_2 full batteries deliver a specific capacity of 200.1 mAh g^{-1} with 82.2% retention after 800 cycles. Large-size pouch-type battery with zinc-deposited *g'*-Ag/*g*-PSiO_x-NH_2/CP anode and high-loading MnO_2 cathode (~15 mg cm^{-2}) also exhibit good rate capability and cyclability. This scalable strategy offers a feasible solution to develop high-durability rechargeable metal-based batteries.

INTRODUCTION

Aqueous zinc-ion batteries (AZIBs) present a compelling option for large-scale energy storage due to their excellent safety and cost-effectiveness. However, as an essential component in AZIBs, the zinc metal anode suffers from disordered dendrite growth, interfacial passivation, and a series of corrosion side reactions, resulting in low Coulombic efficiency (CE) and poor cycle stability (*1*–*3*). Therefore, ensuring homogeneous electro-deposition/stripping of zinc metal has emerged as a bottleneck for the development of practical AZIBs.

Recently, numerous strategies have been proposed to enhance the durability of Zn anodes, such as the construction of artificial solid electrolyte interphase (SEI) (*4*–*7*), the introduction of electrolyte additives (*8*–*11*), and the optimization of the electrode structure (*12*–*16*). Among these approaches, constructing 3D zinc host matrices with high porosity offers a promising solution to achieve guided zinc deposition and extended cycle life. In principle, the high specific surface area lowers the local current density and provides abundant surface sites for Zn nucleation, which helps homogenize Zn^{2+} ion flux and suppress dendrites. Additionally, the porous structure alleviates the Zn^{2+} concentration gradient and accommodates volume changes during cycling, particularly at high current densities or areal capacities (*17*–*22*). Nevertheless, conventional uniform 3D hosts often suffer from a scarcity of accessible nucleation sites within their interior, leading to preferential Zn deposition on the upper surface (referred to as "top growth"). This uneven nucleation fosters dendrite formation and diminishes space utilization. Moreover, the weak binding effect between the conventional uniform 3D host and deposited Zn metal might cause the shedding and accumulation of dead Zn. Gradient designs in 3D Zn anodes address these fundamental limitations by creating a directional driving force for Zn^{2+} transport, guiding preferential Zn nucleation and deposition from the bottom toward the top of the host. This fundamental difference enables full utilization of the 3D framework, facilitating charge transport and electrode reaction at the bottom to deliver superior performance metrics unattainable with conventional or uniform 3D anodes (*23*–*28*). However, it is still challenging to develop 3D host frameworks that simultaneously possess multiple functional gradients (such as porosity, zincophilicity, hydrophobicity, and conductivity) for achieving highly durable zinc metal anodes with controllable zinc plating/stripping behavior.

Herein, we propose the in situ construction of 3D confined host frameworks with multi-component gradients that induce a stack-type zinc plating/stripping behavior, enabling a unique "first-in/last-out" mode. Through an in situ self-assembly approach, the 3D porous scaffold of carbon paper (CP) was successively modified by hydrophobic amino-functionalized polysilane passivation layer (*g*-PSiO_x-NH_2) and conductive zincophilic Ag nanoparticles (*g'*-Ag) to form opposite concentration gradients, denoted as *g'*-Ag/*g*-PSiO_x-NH_2/CP. The concentration gradient distribution of hydrophobic *g*-PSiO_x-NH_2 with –NH_2 terminal groups on CP effectively inhibits anodic corrosion, hydrogen evolution, and promotes the desolvation of Zn^{2+} ions, suppressing the "top-growth" mode of zinc dendrites. Simultaneously, the inverse concentration gradient distribution of conductive and zincophilic *g'*-Ag nanoparticles can guide Zn^{2+} ions to preferentially nucleate at the bottom, and a 3D carbon skeleton mitigates volume expansion during long-term plating/stripping. This collaborative design effectively optimizes the electric field distribution, Zn^{2+} ion flux, and Zn deposition pathway, significantly improving ion/electron

[1]State Key Laboratory of Coordination Chemistry, MOE Key Laboratory of Mesoscopic Chemistry, MOE Key Laboratory of High Performance Polymer Materials and Technology, Jiangsu Key Laboratory of Green Energy Catalysis and Intelligent Chemical Engineering, Suzhou Key Laboratory of Green Intelligent Manufacturing of New Energy Materials and Devices, Tianchang New Materials and Energy Technologies Research Center, Institute of Green Chemistry and Engineering, School of Chemistry and Chemical Engineering, Nanjing University, Nanjing, Jiangsu 210023, P. R. China. [2]School of Chemistry and Chemical Engineering, Suzhou University, Suzhou, Anhui 234000, P. R. China. [3]State Key Laboratory of Structural Analysis, Optimization and CAE Software for Industrial Equipment, Dalian University of Technology, Dalian 116024, China.
*Corresponding author. Email: zhongjin@nju.edu.cn

transport kinetics and enhancing rate capability. Consequently, the zinc-deposited *g*'-Ag/*g*-PSiO$_x$-NH$_2$/CP host electrode (denoted as Zn/*g*'-Ag/*g*-PSiO$_x$-NH$_2$/CP) achieved a high CE and exceptionally long cycling stability, which can be stably cycled for 5000 hours at 10 mA cm^{-2}/10 mAh cm^{-2}, far exceeding the non-gradient (Bare CP) and single-gradient (*g*-PSiO$_x$-NH$_2$/CP and *g*'-Ag/CP) counterparts. Furthermore, full batteries assembled with MnO_2 cathode exhibited a considerable specific capacity of 200.1 mAh g^{-1} with an impressive capacity retention rate of 82% after 800 cycles. To further confirm its practicability, large-size (6 × 7 cm^2) pouch-type Zn||MnO_2 batteries based on Zn/*g*'-Ag/*g*-PSiO$_x$-NH$_2$/CP anode and high-loading MnO_2 cathode (~15 mg cm^{-2}) were fabricated and delivered a specific capacity of 98.9 mAh g^{-1} at 1.0 A g^{-1} after 350 cycles. The multi-component gradients 3D host design achieves spatially partitioned synergy and mechanistic integration, enabling dendrite-free and highly durable zinc anodes and presenting a viable, scalable approach for grid-scale aqueous energy storage.

RESULTS

Design, preparation, and characterizations of *g'*-Ag/*g*-PSiO$_x$-NH$_2$/CP host

The preparation process and 3D nanostructures of *g*'-Ag/*g*-PSiO$_x$-NH$_2$/CP host are illustrated in Fig. 1A. Initially, the bare CP served as the matrix, consisting of interconnected carbon fibers with a diameter of 6–10 μm (fig. S1), which provided a robust scaffold and sufficient porosity to accommodate Zn deposition. First, the *g*-PSiO$_x$-NH$_2$/CP was fabricated by an in situ self-assembly step via the preferential impregnation of (3-aminopropyl)triethoxysilane (APTES) solution, as shown in fig. S2. The PSiO$_x$-NH$_2$ with a concentration gradient was wrapped on

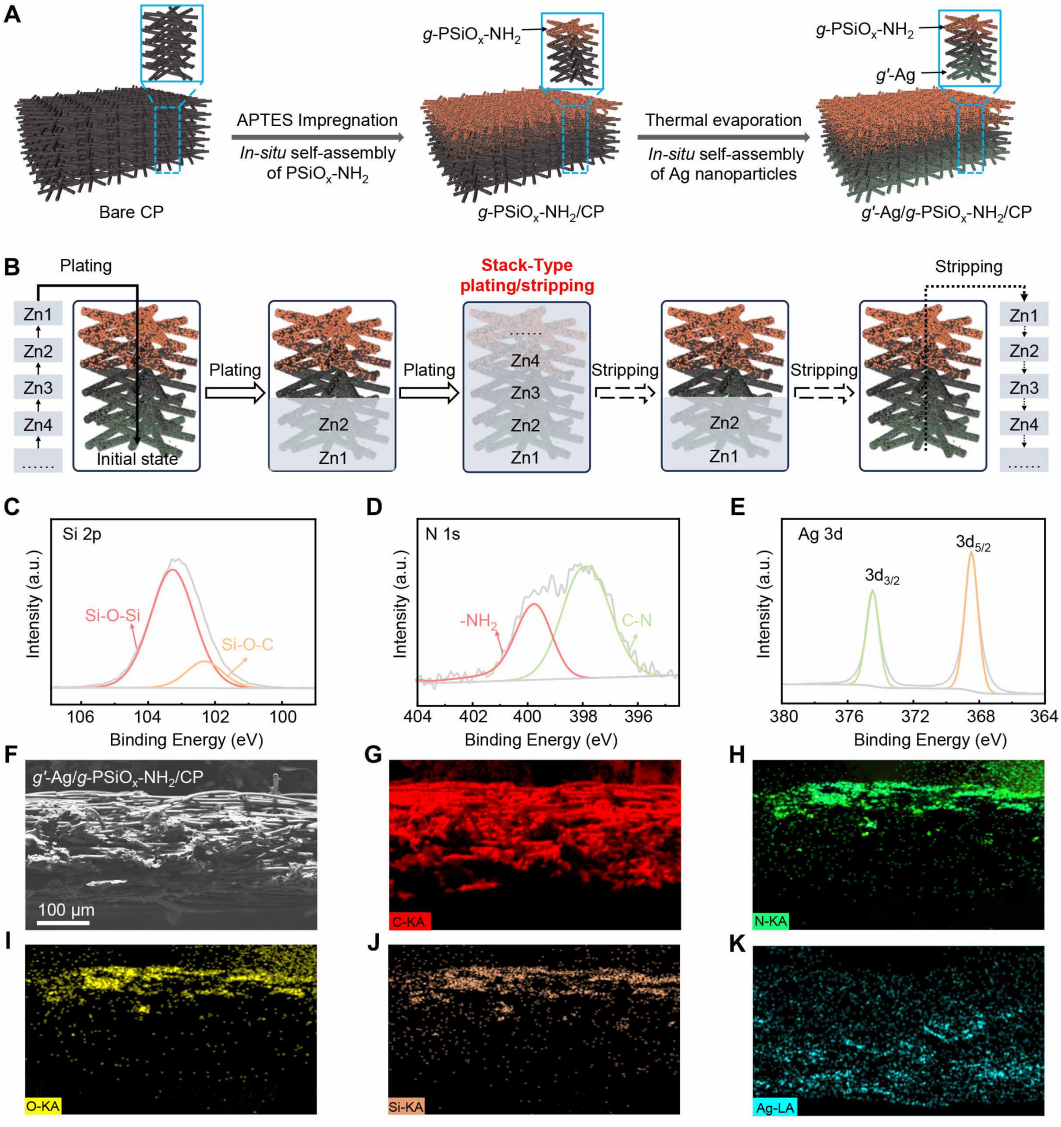

Fig. 1. Construction and characterizations of *g'*-Ag/*g*-PSiO$_x$-NH$_2$/CP host. (**A**) Schematic diagram for the fabrication of *g*'-Ag/*g*-PSiO$_x$-NH$_2$/CP host via a two-step self-assembly approach. (**B**) Schematic illustration of the stack-type zinc plating/stripping behavior with a "first-in/last-out" mode enabled by the *g*'-Ag/*g*-PSiO$_x$-NH$_2$/CP host. (**C** to **E**) High-resolution XPS spectra at Si 2p, N 1 s, and Ag 3d levels of *g*'-Ag/*g*-PSiO$_x$-NH$_2$/CP host. (**F** to **K**) Cross-sectional SEM and corresponding EDS elemental mappings of *g*'-Ag/*g*-PSiO$_x$-NH$_2$/CP host.

the carbon fibers and distributed along the concentration gradient in the cross-section direction of CP. Thereafter, the *g*'-Ag/*g*-$PSiO_x$-NH_2/CP was obtained by another in situ self-assembly step to decorate conductive and zincophilic Ag nanoparticles with an inverse concentration gradient through thermal evaporation of Ag metal (fig. S3). This multi-component gradients in 3D host frameworks can induce a controllable stack-type zinc plating/stripping behavior, as shown in Fig. 1B, displaying the characteristics of a unique "first-in/last-out" zinc plating/stripping mode with significantly improved homogeneity. Moreover, such a deliberate transition structure optimizes the Zn^{2+} ion diffusion pathway in the 3D framework, enabling stable and rapid transmission even under high current densities.

In the XRD pattern of *g*'-Ag/*g*-$PSiO_x$-NH_2/CP (fig. S4), a peak around 26.2° was attributed to the (002) crystal plane of CP, while another peak at approximately 38.2° signified the (111) crystal plane of Ag nanoparticles. Conversely, $PSiO_x$-NH_2 appeared amorphous. In the FT-IR spectra (fig. S5), the peaks at 3445 cm^{-1} (stretching vibration of N–H and O–H), 1632 cm^{-1} (bending vibration of N–H), and 1065 cm^{-1} (stretching vibration of O–Si–O) demonstrated the presence of $PSiO_x$-NH_2 (*29*). The surface compositions of *g*'-Ag/*g*-$PSiO_x$-NH_2/CP were further elucidated by x-ray photoelectron spectroscopy (XPS) (Fig. 1, C to E). The Si 2p spectrum exhibited a robust and broad Si–O peak, which can be deconvoluted into two peaks, Si–O–Si (103.8 eV) and Si–O–C (102.6 eV) in siloxane (*30*). The N 1 s spectrum presented the existence of $–NH_2$ (399.8 eV), which can improve the hydrophobicity of the 3D host (*31*). In the O 1 s spectrum (fig. S6), the presence of Si–O–Si (533.3 eV) and –OH (532.2 eV) was demonstrated. In Ag 3D spectrum (Fig. 1E), the two prominent peaks observed at 368.3 eV and 374.2 eV correspond to Ag $3d_{5/2}$ and Ag $3d_{3/2}$, respectively (*32*). Scanning electron microscopy (SEM) and corresponding energy dispersive spectroscopy (EDS) elemental mappings (Fig. 1, F to K) of as-prepared *g*'-Ag/*g*-$PSiO_x$-NH_2/CP host revealed distinct spatial distributions of various elements: Si and O elements were concentrated in the top layer region, while Ag nanoparticles presented an increasing distribution from top to bottom. This multi-component gradient design establishes a functional gradient field within the electrode through continuous variation in composition and structure, enabling active and precise regulation of key physicochemical processes such as ion flux, electric field distribution, and interfacial reactions. Consequently, it guides the uniform Zn deposition, enhances charge transfer kinetics, and significantly extends cycling lifespan. This architecture spatially coordinates previously incompatible functions, thereby enabling systematic optimization of electrode performance.

Side reaction inhibition and dendrite-free Zn deposition

Corrosion and hydrogen evolution are common occurrences on conventional Zn anodes in aqueous electrolytes, which are closely related to active water and the hydrophilicity of the electrode. In Fig. 2A, 2.0 M $ZnSO_4$ aqueous electrolyte was applied to different hosts for a contact angle test. The *g*'-Ag/*g*-$PSiO_x$-NH_2/CP host exhibited the largest contact angle (128.3°) among all samples, demonstrating its strong hydrophobicity. This high hydrophobicity is primarily attributed to the rough and porous surface morphology created by the *g*-$PSiO_x$-NH_2 layer uniformly coating the carbon fibers (fig. S2). Such a rough surface provides physical shielding that hinders the accumulation of active water molecules within the 3D host. In addition, the intrinsic hydrophobicity of the –O–Si–O– network within the *g*-$PSiO_x$-NH_2 further contributes to the high contact angle (*29*). The *g*'-Ag layer also makes a minor additional contribution by further increasing the surface roughness, as evidenced by the contact angle increase from 125.2° (without Ag) to 128.3° (with Ag). Together, these factors endow the host with excellent surface hydrophobicity. The Tafel tests further evaluated the corrosion resistances of these hosts, as shown in Fig. 2B. The corrosion potential of *g*'-Ag/*g*-$PSiO_x$-NH_2/CP (−0.021 V vs. Zn/Zn^{2+}) is more positive than that of bare CP (−0.0863 V vs. Zn/Zn^{2+}), indicating a lower tendency for hydrogen and oxygen reduction reactions. Moreover, the corrosion current density serves as a more direct indicator for assessing self-corrosion rates. The corrosion current densities of both *g*-$PSiO_x$-NH_2/CP and *g*'-Ag/*g*-$PSiO_x$-NH_2/CP were significantly reduced compared to those of bare CP and *g*'-Ag/CP. This reduction highlighted the good anti-corrosion capability of the *g*-$PSiO_x$-NH_2 coating layer.

The nucleation overpotentials of bare CP, *g*-$PSiO_x$-NH_2/CP, *g*'-Ag/CP and *g*'-Ag/*g*-$PSiO_x$-NH_2/CP electrodes were measured (Fig. 2C). The *g*'-Ag/*g*-$PSiO_x$-NH_2/CP exhibited the lowest nucleation overpotential of 12.8 mV, a considerable reduction compared to bare CP (36.4 mV), *g*-$PSiO_x$-NH_2/CP (41.3 mV) and *g*'-Ag/CP (17.1 mV), which effectively diminished the nucleation barrier and highlighted the strong zincophilic properties of Ag nanoparticles. Furthermore, to evaluate the evolution behavior of Zn deposition, Zn electro-plating processes on bare Zn foil and various 3D hosts were observed by in situ optical microscopy (Fig. 2, D to F, and fig. S7). The poor resistance to side reactions and the tip effect of bare Zn foil resulted in the rapid formation of thick Zn dendrites (Fig. 2D). Although bare CP possessed a 3D skeleton, the absence of zincophilic nucleation sites led to uneven deposition on the surface, forming mossy zinc dendrites (Fig. 2E). Notably, no uneven protrusions were observed on the *g*'-Ag/*g*-$PSiO_x$-NH_2/CP host, and its hierarchical pores were gradually filled with continuously deposited Zn, eventually forming a uniform and dense composite Zn electrode (Fig. 2F). This controllable Zn deposition behavior effectively can reduce the short-circuit risk caused by dendrite penetration against the separator, thereby promoting the cycling durability at high current densities/large capacities.

Reversible stack-type Zn plating/stripping behavior

To further evaluate the Zn deposition behaviors, the morphology evolutions of the four hosts were observed by ex situ SEM and EDS. In the case of bare CP, the plating/stripping behaviors of Zn are depicted in Fig. 3A. The non-gradient bare CP host framework, possessing spatially uniform conductivity and zincophilic affinity, promotes rapid Zn nucleation and Zn^{2+} ion aggregation at the top surface, where ions traverse the shortest pathway. Consequently, a preferred top Zn deposition process occurred, potentially resulting in an internal short circuit during extended cycling. Figure 3B revealed that the top surface of bare CP framework accumulated substantial Zn and became cluttered after Zn deposition (i.e., Zn/CP), leading to the emergence of slender zinc dendrites with increasing deposition amounts. Additionally, the Zn metal cannot be fully stripped and partially remained on the framework, resulting in low CE. The cross-section SEM images and corresponding overlapped EDS elemental mappings of Zn/CP electrode with different plating/stripping capacities (Fig. 3C) provided a clearer and more intuitive view of Zn deposition, indicating Zn accumulation predominantly on the top surface, leaving virtually no Zn deposition at the bottom. Moreover, the physical appearance of Zn/CP electrode after plating 20 mAh cm^{-2} of Zn metal was displayed in fig. S8, revealing large chunks of unevenly distributed Zn on the top surface. Undoubtedly, such outcomes would result in reduced space utilization within the host framework and inevitably an internal short circuit after long-term cycling.

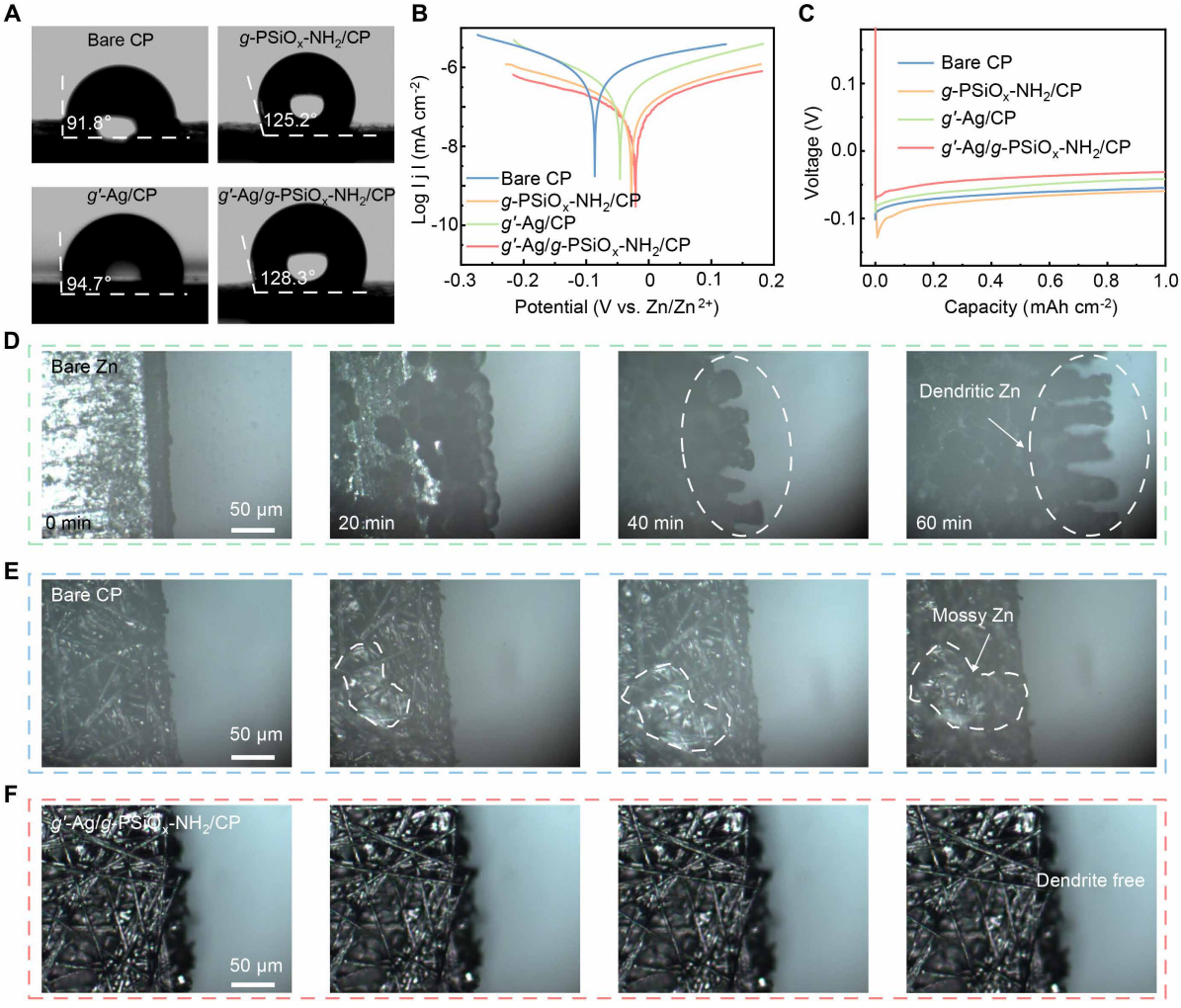

Fig. 2. Interfacial properties and zinc deposition observations. (**A**) Contact angles of 2.0 M $ZnSO_4$ aqueous electrolyte on the surface of different 3D hosts. (**B**) Tafel curves of different 3D hosts. (**C**) Overpotential profiles of these different hosts at 5 mA cm^{-2}. (**D** to **F**) In situ optical microscopy observations of Zn deposition morphologies on (D) bare Zn, (E) bare CP, and (F) *g'*-Ag/*g*-$PSiO_x$-NH_2/CP hosts.

In contrast, the nucleation and plating/stripping behaviors of the *g'*-Ag/*g*-$PSiO_x$-NH_2/CP host were illustrated in Fig. 3D, where Zn preferentially nucleated uniformly on the bottom until filling the entire space by stack-type plating. As the deposition amount increased, the deposition morphology of Zn/*g'*-Ag/*g*-$PSiO_x$-NH_2/CP sharply contrasted with that of the bare CP. As shown in Fig. 3, E and F, there were no large chunks of Zn metal on the top surface even with a deposition of 20 mAh cm^{-2}, but more and more Zn on the bottom. As zincophilic seeds, the Ag nanoparticles offered ample nucleation sites, effectively lowering the nucleation potential barrier and guiding Zn to achieve uniform nucleation rapidly on each surface of carbon fiber. Subsequently, the growth morphology of deposited Zn evolved from initial Zn grains to flat Zn, completely wrapped around each carbon fiber. The inserts in Fig. 3F highlighted the morphology of uniform nucleation and plating of Zn metal during different deposition stages. After Zn stripping, the surface was devoid of any Zn residue and appeared remarkably clean, confirming significantly enhanced CE performance. As evident in Fig. 3G, the Zn element distribution was notably higher at the bottom than at the top during plating. Conversely, Zn at the top surface was preferentially reduced during stripping. This stack-type behavior ("first-in/last-out" or "last-in/first-out") indicates a highly reversible Zn plating/stripping process, which significantly enhances space utilization and cycling stability.

To further confirm the superiority of the multi-component gradient design, we compared the deposition behaviors of Zn metal on single-gradient hosts (*g*-$PSiO_x$-NH_2/CP and *g'*-Ag/CP). Figure S9 illustrated the morphology of Zn deposition on the *g*-$PSiO_x$-NH_2/CP. Notably, deposited Zn formed smaller lumps compared to bare CP and aggregated predominantly below the *g*-$PSiO_x$-NH_2 passivation layer. This phenomenon was attributed to the *g*-$PSiO_x$-NH_2 layer hampering the sufficient contact of Zn^{2+} ions with the surface of CP, as well as increasing the local interfacial impedance of CP. Consequently, Zn^{2+} ions tend to diffuse and deposit on the exposed CP surface not fully shielded by the *g*-$PSiO_x$-NH_2 layer. In stark contrast to bare CP and *g*-$PSiO_x$-NH_2/CP, the *g'*-Ag/CP after Zn deposition shows a remarkably flat morphology in fig. S10, accompanied by a uniform distribution of deposited Zn throughout the framework. Overall, the *g'*-Ag/*g*-$PSiO_x$-NH_2/CP exhibits the best regulation

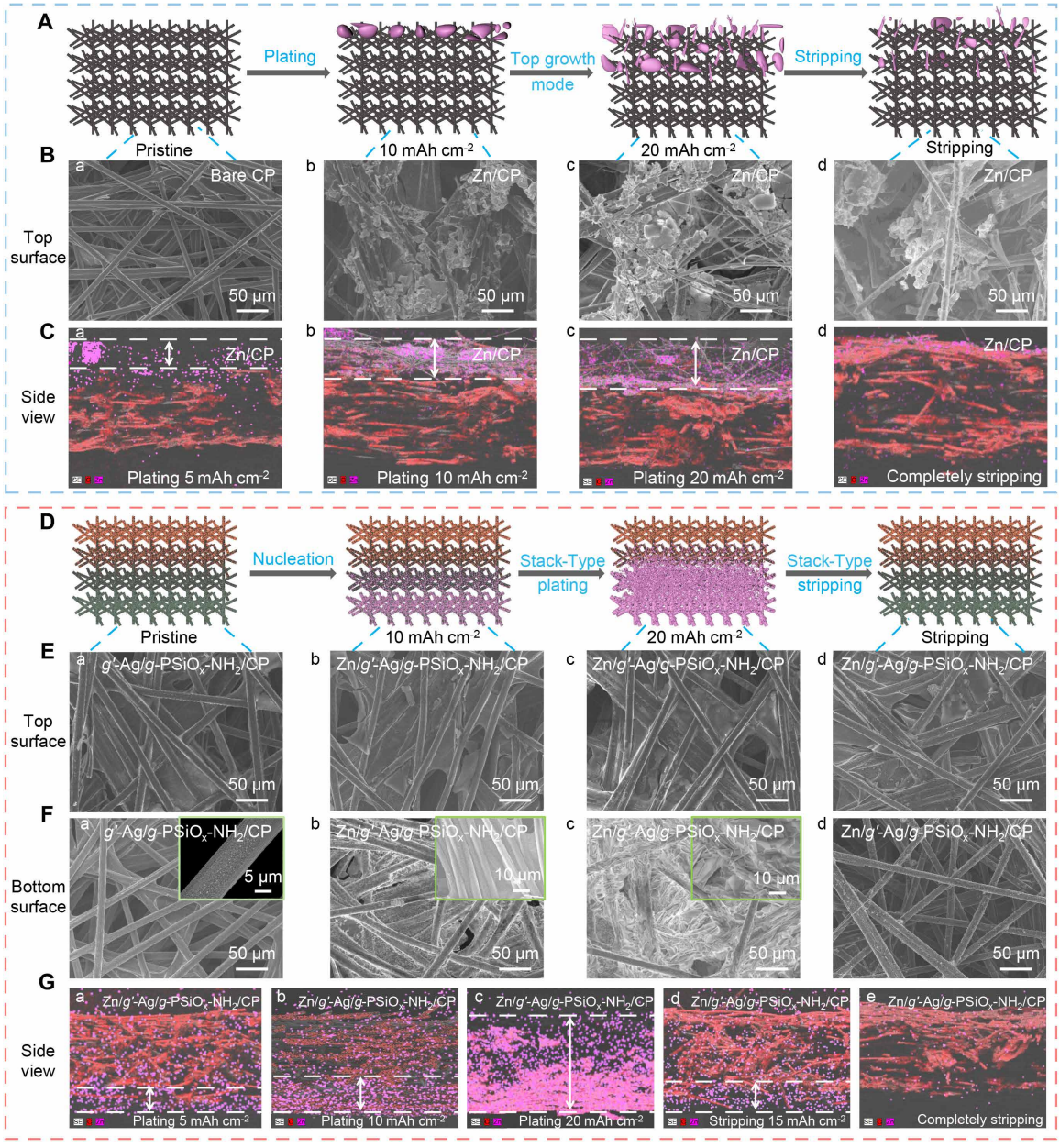

Fig. 3. Zn deposition behavior investigations. (**A**) Schematic of Zn plating/stripping behavior on bare CP host. (**B**) Top surface morphologies of bare CP: (a) at pristine state, (b) plated 10 mAh cm^{-2} of Zn, (c) plated 20 mAh cm^{-2} of Zn, and (d) after completely stripping. (**C**) Cross-section EDS elemental mappings of bare CP with different plating/stripping capacities: (a) plated 5 mAh cm^{-2} of Zn, (b) plated 10 mAh cm^{-2} of Zn, (c) plated 20 mAh cm^{-2} of Zn, (d) after completely stripping. (**D**) Schematic of Zn plating/stripping behavior on *g'*-Ag/*g*-$PSiO_x$-NH_2/CP host. (**E** and **F**) Top and bottom surface morphologies of *g'*-Ag/*g*-$PSiO_x$-NH_2/CP: (a) at pristine state, (b) plated 10 mAh cm^{-2} of Zn, (c) plated 20 mAh cm^{-2} of Zn, and (d) after completely stripping. (**G**) Cross-section EDS elemental mappings of *g'*-Ag/*g*-$PSiO_x$-NH_2/CP with different plating/stripping capacities: (a) plated 5 mAh cm^{-2} of Zn, (b) plated 10 mAh cm^{-2} of Zn, (c) plated 20 mAh cm^{-2} of Zn, (d) stripped 15 mAh cm^{-2} of Zn, and (e) after completely stripping.

capability over Zn nucleation/growth compared to the bare CP, *g*-$PSiO_x$-NH_2/CP and *g*'-Ag/CP counterparts, achieving dendrite-free, uniform, and dense deposition of Zn metal at high capacity.

Theoretical calculation

To clarify the distinct zinc deposition behavior on different hosts, mechanistic insights were obtained through theoretical calculations. Density functional theory (DFT) calculations were employed to investigate the influence of different interlayers on the desolvation process of zinc ions (fig. S11) and the corresponding energy barriers. As shown in Fig. 4A, the *g*-$PSiO_x$-NH_2 passivation layer can effectively reduce the desolvation energy barrier. This is attributed to the ability of its amino groups to form hydrogen bonds with free water molecules, which accelerates the dissociation of coordinated zinc ions, enhances the reaction kinetics, and ultimately leads to a significant reduction in the desolvation energy barrier for zinc ions. In addition, Figure 4B indicates that Zn atoms

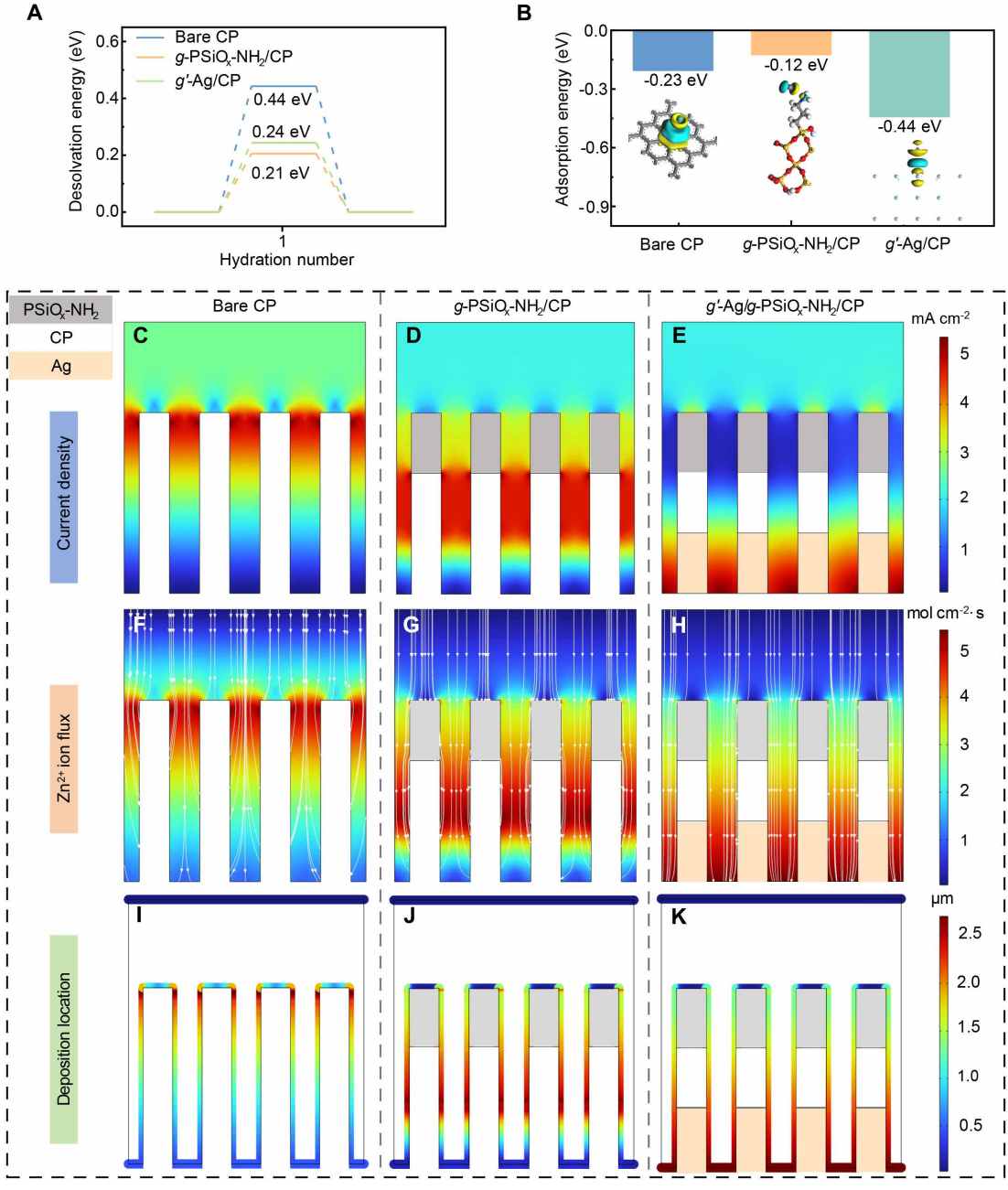

Fig. 4. Studies on Zn^{2+} desolvation and deposition pathways of multi-component gradient hosts. (**A**) DFT-calculated desolvation energy profile Zn^{2+} dehydration on the surfaces of bare CP, *g*-PSiO_x-NH_2/CP, and *g'*-Ag/CP. (**B**) Optimized binding models for Zn on different hosts and the corresponding adsorption energies from DFT calculations. (**C** to **K**) COMSOL simulations of [(C) to (E)] current density, [(F) to (H)] Zn^{2+} ion flux, and [(I) to (K)] deposition location distribution of bare CP, *g*-PSiO_x-NH_2/CP, and *g'*-Ag/*g*-PSiO_x-NH_2/CP.

exhibit stronger binding to the Ag surface (−0.44 eV) compared to bare CP (−0.23 eV) and *g*-PSiO_x-NH_2/CP (−0.12 eV), confirming the enhanced Zn^{2+} affinity and preferred nucleation on Ag nanoparticles. Moreover, the charge density difference revealed that Ag nanoparticles possess a superior electron localization ability, which is conducive to uniform Zn deposition.

To evaluate the rationality of the multi-component gradient designs, simplified equivalent models were established by COMSOL Multiphysics to investigate the effect of gradient properties on the Zn deposition behavior. The current density (Fig. 4, C to E), Zn^{2+} ion flux (Fig. 4, F to H) and deposition location distribution (Fig. 4, I to K) of bare CP, *g*-PSiO_x-NH_2/CP, *g'*-Ag/CP (fig. S12), and *g'*-Ag/*g*-PSiO_x-NH_2/CP hosts were simulated, respectively. On the gradient-free bare CP, owing to its good conductivity and the shorter diffusion path of Zn^{2+} ions on top surface, a higher concentration of current density and Zn^{2+} ion flow in the upper surface area. Consequently, zinc tended to deposit directly onto the surface (Fig. 4I), resulting in dendrite growth and side reactions. Moreover, this deposition

mode may lead to rapid blockage of ion channels, reducing space utilization. In the case of the single-gradient *g*-$PSiO_x$-NH_2/CP, the high current density and high Zn^{2+} ions flux were mainly concentrated in the middle region. This is because the shielding effect and increased interfacial impedance caused by *g*-$PSiO_x$-NH_2 coating layer hampered the deposition of Zn metal on the top surface of *g*-$PSiO_x$-NH_2/CP. In other words, the *g*-$PSiO_x$-NH_2 passivation layer acted as a shield against the high electric field strength of the surface layer, and thereby Zn metal was preferentially deposited on the lower exposed CP surface not completely shielded by the *g*-$PSiO_x$-NH_2 layer. However, Zn^{2+} cannot be selectively deposited on the bottom due to the absence of zincophilic nucleation sites. Therefore, Zn metal was randomly deposited on the middle region beneath the *g*-$PSiO_x$-NH_2 passivation layer (Fig. 4J). Figure 4, E, H, and K presented the simulation results of the *g'*-Ag/*g*-$PSiO_x$-NH_2/CP. With the incorporation of conductive and zincophilic Ag nanoparticles, the Zn^{2+} ions flux was efficiently guided towards the bottom, promoting preferential deposition in this region. This optimization of the deposition pathway enhances reaction kinetics at the bottom of the electrode and prevents the top-deposition mode. Moreover, the simulation results are consistent with the morphology observation by SEM and EDS. This targeted "bottom preferential" stack-type deposition behavior not only achieves uniform, dense, and dendrite-free Zn deposition under high-capacity conditions, but also maximizes space utilization while significantly enhancing cycle stability.

Electrochemical performances of *g'*-Ag/*g*-$PSiO_x$-NH_2/CP

Given the superior Zn deposition characteristics of *g'*-Ag/*g*-$PSiO_x$-NH_2/CP as revealed above, the cycling performance was evaluated and compared with bare CP, *g*-$PSiO_x$-NH_2/CP and *g'*-Ag/CP electrodes by assembling half cells with Zn foil as the counter electrode. As presented in Fig. 5A, the *g'*-Ag/*g*-$PSiO_x$-NH_2/CP electrode exhibited much better cyclic reversibility at different current densities than the other three electrodes, especially at high current densities. Figure 5B showed the voltage-capacity curves of the four electrodes at the 100th cycle, where the *g'*-Ag/*g*-$PSiO_x$-NH_2/CP electrode delivered almost identical charge and discharge capacities, according well with its high CE of above 99.2%. To further evaluate the reversibility under demanding conditions, the CE was also measured at a high areal capacity of 20 mAh cm^{-2}, as shown in fig. S13. The *g'*-Ag/*g*-$PSiO_x$-NH_2/CP host framework delivers a high CE exceeding 98.5% over 300 cycles at 10 mA cm^{-2}/20 mAh cm^{-2}. In contrast, the *g*-$PSiO_x$-NH_2/CP and *g'*-Ag/CP electrodes exhibited obvious fluctuations and rapid decay after 180 cycles, while the bare CP electrode showed even more severe degradation after only 75 cycles. Furthermore, even at a higher current density of 20 mA cm^{-2}, the *g'*-Ag/*g*-$PSiO_x$-NH_2/CP maintained stable cycling for over 200 cycles, demonstrating superior deposition/stripping reversibility compared to the other control samples. Remarkably, the CE of *g'*-Ag/*g*-$PSiO_x$-NH_2/CP is also superior to most of the recently reported 3D gradient hosts under similar testing conditions (table S1) (*20, 33–41*). To investigate the interfacial charge-transfer kinetics, electrochemical impedance spectroscopy (EIS) was performed on symmetric cells assembled by preloading a certain amount of Zn on these hosts (fig. S14). The Zn/*g'*-Ag/*g*-$PSiO_x$-NH_2/CP symmetric cell consistently exhibited the lowest charge-transfer resistance before and after cycling, indicating favorable interfacial compatibility and efficient charge transfer enabled by the multi-component gradient architecture. The voltage hysteresis and galvanostatic cycling stability of these symmetric cells were also investigated, as shown in Fig. 5, C and D, and figs. S15 to S18. The Zn/*g'*-Ag/*g*-$PSiO_x$-NH_2/CP symmetric cell could exhibit an ultralong stable cycling over 6000 hours with a smaller voltage hysteresis at 1 mA cm^{-2}/1 mAh cm^{-2}. In contrast, the other three types symmetrical cells showed larger voltage hysteresis and fluctuations after 1000 hours (Fig. 5C). It is worth noting that the advantage of Zn/*g'*-Ag/*g*-$PSiO_x$-NH_2/CP was more obvious at a high current density, with an ultra-long cycle life of 5000 hours at 10 mA cm^{-2}, far exceeding the non-gradient and single-gradient electrodes (Fig. 5D and fig. S17). The high-areal-capacity performance was further evaluated at 20 mAh cm^{-2} (fig. S18). At 10 mA cm^{-2}, the Zn/*g'*-Ag/*g*-$PSiO_x$-NH_2/CP symmetric cell achieved stable cycling for more than 3000 hours with relatively low and consistent voltage hysteresis. In sharp contrast, other control cells (Zn/*g'*-Ag/CP, Zn/*g*-$PSiO_x$-NH_2/CP, and Zn/CP) failed much earlier at approximately 2000 hours, 1800 hours, and 1000 hours, respectively, all exhibiting progressive polarization buildup during cycling. Even at 20 mA cm^{-2}, the Zn/*g'*-Ag/*g*-$PSiO_x$-NH_2/CP maintained stable operation over 2500 hours, demonstrating its robustness under extreme conditions. Rate performance tests (Fig. 5E) revealed that the Zn/*g'*-Ag/*g*-$PSiO_x$-NH_2/CP electrode could maintain stable cycling as the current density increases sequentially, and significantly lower voltage hysteresis compared to other electrodes. Impressively, the electrochemical performances of Zn/*g'*-Ag/*g*-$PSiO_x$-NH_2/CP, including current density, voltage hysteresis, and cycling lifespan, are very competitive compared to other 3D gradient hosts reported in previous literature (Fig. 5F and table S2) (*33–45*).

To more directly evaluate the Zn deposition/stripping reversibility and the interfacial stability of different electrodes during cycling, the surface morphologies of symmetric cells using Zn/CP, Zn/*g*-$PSiO_x$-NH_2/CP, Zn/*g'*-Ag/CP, and Zn/*g'*-Ag/*g*-$PSiO_x$-NH_2/CP electrodes were characterized by SEM after 100, 200, and 300 cycles, respectively, as shown in fig. S19. The Zn/CP electrode exhibited progressive reversibility degradation with increasing cycle number. After 200 cycles, Zn dendrites began to appear on the surface, while by 300 cycles, the surface was densely covered with abundant flaky Zn deposits and pronounced dendrites, indicating a rapid decline in reversibility. In contrast, the Zn/*g*-$PSiO_x$-NH_2/CP electrode maintained a clean surface across all cycling stages, with no observable dendrites or residual Zn, confirming that the $PSiO_x$-NH_2/CP passivation layer suppressed irregular Zn deposition and dendrite formation on the top surface. The Zn/*g'*-Ag/CP electrode showed an overall tidy morphology with only sporadic Zn particles remaining on the carbon fibers, suggesting that Ag nanoparticles improved the uniformity of Zn plating and stripping. Notably, the Zn/*g'*-Ag/*g*-$PSiO_x$-NH_2/CP electrode displayed no visible dendrites or Zn accumulation throughout all examined cycles. These results further demonstrate the pronounced advantage of the multi-component gradient design in stabilizing the Zn anode interface, inhibiting dendrite growth, and enhancing cycling reversibility.

To further evaluate the practicability of the Zn/*g'*-Ag/*g*-$PSiO_x$-NH_2/CP anode, full batteries were assembled with MnO_2 loaded on CP (MnO_2/CP) as cathode (Fig. 6A, figs. S20 and S21). The cyclic voltammetry (CV) curves of different full batteries (Fig. 6B) exhibited two distinct redox peaks at 1.22/1.38 V and 1.52/1.58 V, corresponding to the insertion and extraction of Zn^{2+} in the MnO_2 cathode. Compared to other three samples, the Zn/*g'*-Ag/*g*-$PSiO_x$-NH_2/CP anode displayed sharper redox peaks, lower polarization voltage and higher response current, indicating enhanced reaction reversibility and faster ion/electron transport kinetics. Consequently, the Zn/*g'*-Ag/*g*-$PSiO_x$-NH_2/CP||MnO_2/CP battery delivered a higher reversible capacity of 300.1 mAh g^{-1} at 0.2 A g^{-1}, which is considerably

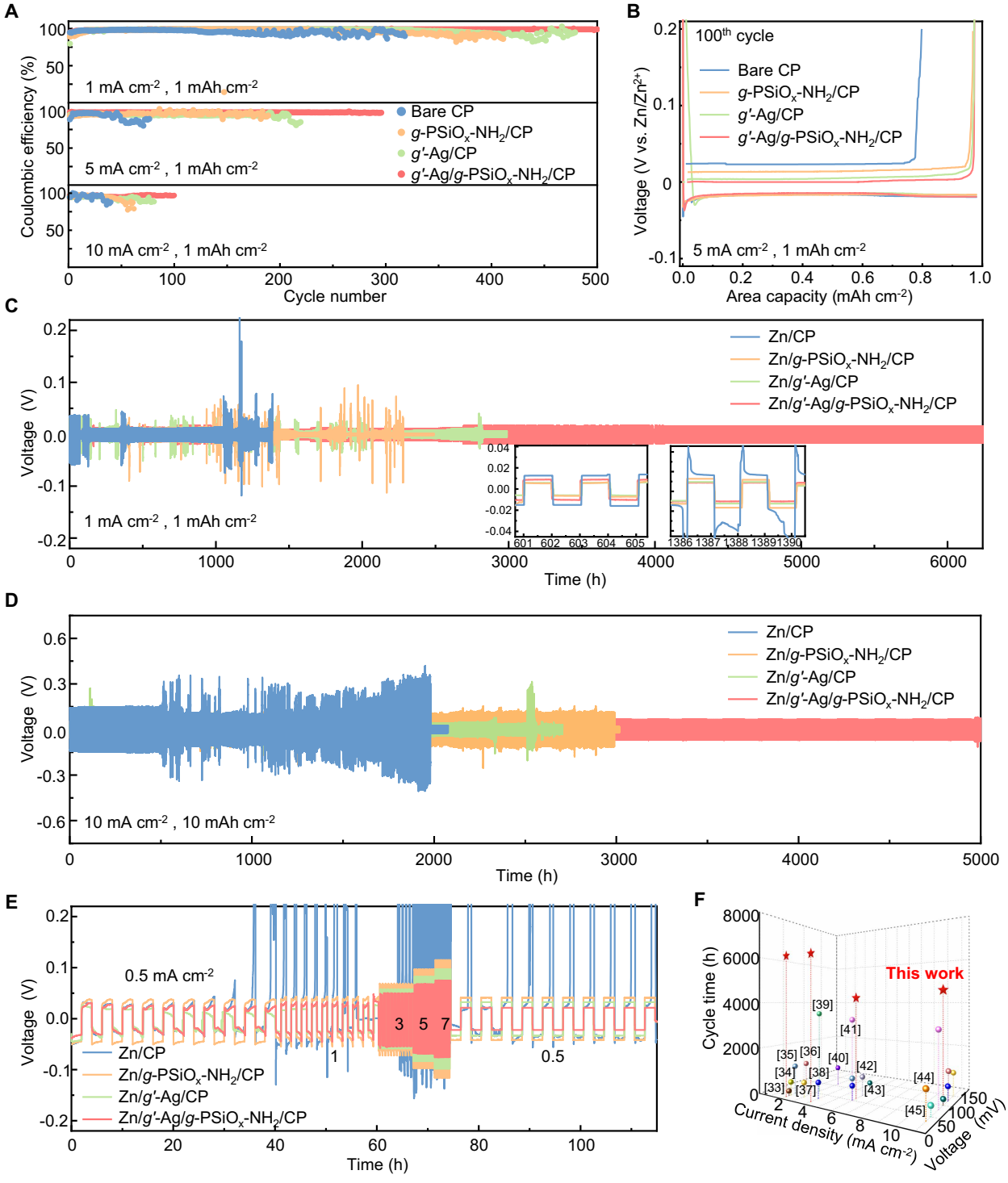

Fig. 5. Electrochemical performances of different Zn host electrodes. (**A**) CEs of the bare CP, *g*-PSiO$_x$-NH$_2$/CP, *g'*-Ag/CP and *g'*-Ag/*g*-PSiO$_x$-NH$_2$/CP host electrodes at different current densities. (**B**) Voltage-capacity curves of different Zn host electrodes at the 100th cycle. (**C** and **D**) Galvanostatic cycling performance of the symmetric cells with different host electrodes at 1 mA cm^{-2}/1 mAh cm^{-2} and 10 mA cm^{-2}/10 mAh cm^{-2}. (**E**) Rate performance of the symmetric cells with different Zn host electrodes. (**F**) Comparison of the current density, voltage hysteresis and cycling lifespan of the *g'*-Ag/*g*-PSiO$_x$-NH$_2$/CP host electrode with other 3D gradient hosts reported in previous literature (*33*–*45*).

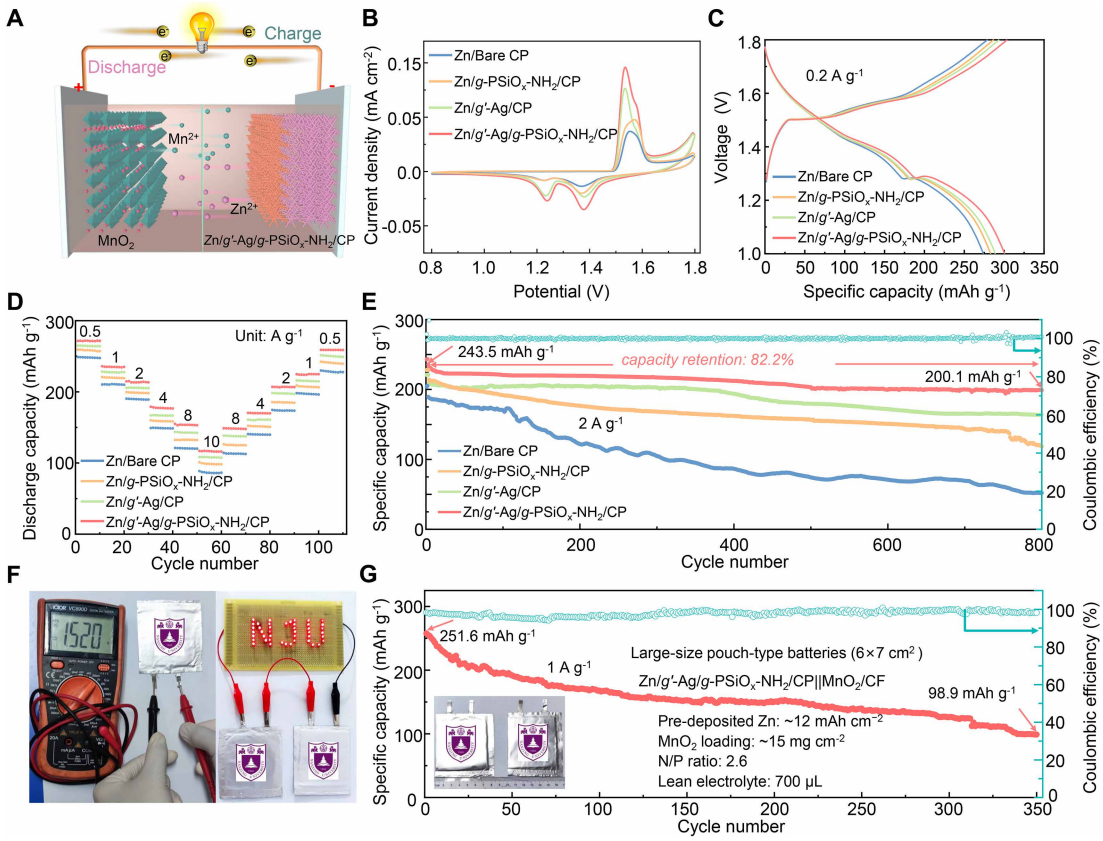

Fig. 6. Electrochemical performances of full batteries and large-size pouch-type batteries. (**A**) Schematic configuration of the Zn/*g'*-Ag/*g*-PSiO_x-NH_2/CP||MnO_2 full battery system. (**B**) CV curves of different full batteries during the second cycle. (**C**) Charge-discharge curves of different full batteries at 0.2 A g^{-1}. (**D**) Rate performance and (**E**) Long-term cycling stability of different full batteries at 2 A g^{-1}. (**F**) Photographs of large-size pouch-type Zn/*g'*-Ag/*g*-PSiO_x-NH_2/CP||MnO_2/CF batteries for (left) open circuit voltage test and (right) lighting up an LED panel. (**G**) Cycling stability of large-size pouch-type Zn/*g'*-Ag/*g*-PSiO_x-NH_2/CP||MnO_2/CF batteries at 1 A g^{-1}.

superior to those of the Zn/CP||MnO_2/CP (273.3 mAh g^{-1}), Zn/*g*-PSiO_x-NH_2/CP||MnO_2/CP (283.2 mAh g^{-1}), and Zn/*g*'-Ag/CP||MnO_2/CP (288.4 mAh g^{-1}) batteries (Fig. 6C). Figure 6D demonstrated that the specific capacity of the Zn/*g*'-Ag/*g*-PSiO_x-NH_2/CP||MnO_2/CP battery was higher than those of other three prototypes under different rates. It still provided a specific capacity of ~127.3 mAh g^{-1} even at 10 A g^{-1}, outperforming the Zn/CP||MnO_2/CP (~70.6 mAh g^{-1}), Zn/*g*-PSiO_x-NH_2/CP||MnO_2/CP (~98.4 mAh g^{-1}), and Zn/*g*'-Ag/CP||MnO_2/CP (~106.3 mAh g^{-1}) batteries. Furthermore, as shown in fig. S22, the Zn||MnO_2 full cell with the Zn/*g*'-Ag/*g*-PSiO_x-NH_2/CP anode exhibited the smallest voltage polarization among all tested anodes across various current densities (1, 2, 4, 8, and 10 A g^{-1}). In contrast, the Zn/*g*-PSiO_x-NH_2/CP, Zn/*g*'-Ag/CP and Zn/CP anodes show progressively larger voltage gaps between charge and discharge platforms, especially at higher rates. These results confirm that multi-component gradients design effectively mitigates polarization and maintains good rate capability even under high current densities. Figure 6E further tested the long cycle life of four different full batteries at a high current density of 2 A g^{-1}. Impressively, the specific capacity of Zn/*g*'-Ag/*g*-PSiO_x-NH_2/CP||MnO_2/CP battery was initially 243.5 mAh g^{-1}, and maintained at 200.1 mAh g^{-1} after 800 cycles, with a high capacity-retention rate of 82.2%, markedly exceeding the values of the Zn/CP||MnO_2/CP (~61.9 mAh g^{-1}), Zn/*g*-PSiO_x-NH_2/CP||MnO_2/CP (~120.6 mAh g^{-1}), and Zn/*g*'-Ag/CP||MnO_2/CP (~163.7 mAh g^{-1}), further confirming the superior electrochemical stability of the integrated Zn/*g*'-Ag/*g*-PSiO_x-NH_2/CP anode.

Encouraged by these results, pouch-type batteries with a large-size of 6 × 7 cm^2 were further assembled by Zn/*g*'-Ag/*g*-PSiO_x-NH_2/CP anode with pre-deposited Zn of 12 mAh cm^{-2}, MnO_2 loaded carbon felt (MnO_2/CF) cathode with a MnO_2 loading of 15 mg cm^{-2}, low negative/positive capacity ratio (N/P ≈ 2.6), and lean electrolyte (700 μl). The pouch-type Zn/*g*'-Ag/*g*-PSiO_x-NH_2/CP||MnO_2/CF batteries exhibited a high open circuit voltage of 1.52 V, and a LED panel could be lit by only two series-connected batteries (Fig. 6F). Furthermore, the electrochemical performances of the pouch-type batteries were tested under practical conditions. The pouch-type Zn/*g*'-Ag/*g*-PSiO_x-NH_2/CP||MnO_2/CF batteries showed an initial specific capacity of 251.6 mAh g^{-1}, and still maintained at 98.9 mAh g^{-1} after 350 cycles at 1 A g^{-1} (Fig. 6G). These results confirm the promising potential of *g*'-Ag/*g*-PSiO_x-NH_2/CP host electrode for practical application in large-size pouch-type AZIBs.

DISCUSSION

In summary, we propose a feasible strategy for the in situ construction of 3D multi-component gradient hosts that enables a stack-type zinc plating/stripping behavior with a controllable and rapid "first-in/last-out" mode. As revealed by experimental characterizations

and theoretical calculations, the *g*-PSiO$_x$-NH$_2$ passivation layer accelerates the de-solvation of hydrated Zn^{2+}, promoting rapid ion diffusion kinetics and suppressing side reactions. Furthermore, the *g'*-Ag nanoparticles regulate Zn^{2+} ion flux for preferential nucleation at the bottom region, while the 3D porous CP framework accommodates volume variation. This synergy collectively enables uniform Zn deposition/plating and stable cycling of *g'*-Ag/*g*-PSiO$_x$-NH$_2$/CP host. Consequently, the *g'*-Ag/*g*-PSiO$_x$-NH$_2$/CP electrode exhibited desirable Zn deposition behavior and superior electrochemical performances, including a lower overpotential (12.8 mV), a higher Coulombic efficiency (~99.2%), and a longer cycling stability (6000 hours), far exceeding other 3D gradient hosts reported in previous studies. Moreover, by employing this multi-component gradient design strategy on Zn anodes, the Zn||MnO_2 full batteries and scaled-up pouch-type batteries demonstrated good rate capability, considerable capacity retention and significantly prolonged cycling lifespan. Given its high adaptability, this multi-component gradient-induced stack-type deposition mode is expected to be widely applicable in various secondary battery systems plagued by dendrite growth. This study pioneers a universal design principle for next-generation energy storage systems—spanning from scalable AZIBs to cross-domain applications in other metal batteries—promising to redefine the boundaries of electrochemical energy storage and promote the transition toward sustainable energy architectures.

MATERIALS AND METHODS

Chemicals and materials

(3-aminopropyl)triethoxysilane (APTES), polyvinylidene difluoride (PVDF), N-methyl-2-pyrrolidone (NMP) and $ZnSO_4{\cdot}7H_2O$ were purchased from Shanghai Aladdin Biochemical Technology Co., Ltd. Carbon paper (CP), carbon felt (CF) and ketjen black (KB, ECP600JD) were purchased from Suzhou Sinero Technology Co., Ltd. Whatman separator (Catalog No. 1820–047) and zinc foil with a thickness of 0.1 mm were purchased from Nanjing WANQING Chemical Glass Ware & Instrument Co. Ltd. All materials were directly used without further purification.

Preparation of 3D multi-component gradient hosts

Prior to the modification of amino-functionalized polysilane (*g*-PSiO$_x$-NH$_2$) self-assembly layer with a concentration gradient on a piece of CP, the bottom of CP was covered with tape to protect it from the reactions. Then, the CP was immersed in an anhydrous ethanol solution of 1.0 vol.% APTES at 60°C for 30 min, and dried under vacuum at 60°C for 2 hours, to yield the *g*-PSiO$_x$-NH$_2$/CP host. After that, the covering tape was peeled off, and the *g*-PSiO$_x$-NH$_2$/CP host with the bottom facing upwards was placed in a thermal evaporation vacuum chamber. Subsequently, *g'*-Ag nanoparticles with an inverse concentration gradient were evaporated on the bottom of CP with an evaporation rate of 1 Å/s until reaching an average thickness of 20 nm, to yield a multi-component gradient host, i.e. *g'*-Ag/*g*-PSiO$_x$-NH$_2$/CP.

As two control samples, *g*-PSiO$_x$-NH$_2$/CP and *g'*-Ag/CP hosts were also prepared. These were synthesized by omitting the *g'*-Ag modification and the *g*-PSiO$_x$-NH$_2$/CP modification steps, respectively.

Preparation of multi-component gradient host confined Zn anodes

An electrodeposition method was used to fabricate composite Zn anode confined in the multi-component gradient hosts. Briefly, a beaker battery was assembled using a specific 3D host framework (such as bare CP, *g*-PSiO$_x$-NH$_2$/CP, *g'*-Ag/CP, and *g'*-Ag/*g*-PSiO$_x$-NH$_2$/CP) as the working electrode, a piece of zinc foil as the counter electrode, and 2.0 M $ZnSO_4$ as the aqueous electrolyte. Through galvanostatic discharging at 5 mA cm^{-2} for 2 hours or 4 hours, a multi-component gradient confined Zn anode could be obtained, corresponding to an areal capacity of 10 or 20 mAh cm^{-2}, respectively. The Zn-deposited electrodes were denoted as Zn/CP, Zn/*g*-PSiO$_x$-NH$_2$/CP, Zn/*g'*-Ag/CP, and Zn/*g'*-Ag/*g*-PSiO$_x$-NH$_2$/CP, accordingly.

Preparation of MnO_2/CP and MnO_2/CF cathodes

The MnO_2/CP cathode was prepared by the hydrothermal deposition of MnO_2 active material on CP current collector. Briefly, 67 mg of $KMnO_4$ and 0.5 ml of 6 M HCl solution were dissolved in 60 ml of deionized water to form a uniform solution in a 100 ml Teflon-lined stainless-steel hydrothermal autoclave. Subsequently, a piece of CP was immersed into the solution. The hydrothermal autoclave was sealed and maintained at 85°C for 20 mins to yield a MnO_2/CP cathode with an areal MnO_2 loading of ~1.2 mg cm^{-2}.

For the preparation of high-loading MnO_2/CF cathode, MnO_2 active material was firstly prepared separately. Briefly, 0.658 g of $KMnO_4$ and 2.4 ml of 6 M HCl solution were added into 76 ml of deionized water and magnetic stirred for 10 min. The mixture was transferred into a 100 ml hydrothermal autoclave. The hydrothermal autoclave was sealed and maintained at 140°C for 10 hours. The mixture was centrifuged and cleaned after cooling, the brown solid powder was collected and vacuum dried at 60°C for 12 hours to obtain MnO_2 active material. Then, MnO_2 active material, KB and PVDF were mixed with NMP solvent at a weight ratio of 8:1:1. The slurry was coated on a piece of 6×7 cm^2 CF and dried in a vacuum oven at 60°C for 6 hours to obtain a high-loading (~15 mg cm^{-2}) MnO_2/CF cathode.

Material characterizations

The morphological and structural characterizations were performed by SEM (FEI Nano-450, with an accessory EDX spectrometer). XRD data was collected on Shimadzu 6000 x-ray diffractometer with a Cu Kα radiation source (λ = 1.54178 Å). X-ray photoelectron spectra (XPS) were acquired on a PHI-5000 VersaProbe with an Al Kα x-ray radiation source. Fourier transform infra-red (FT-IR) spectra were recorded on a Bruker Tensor 27 spectrometer by 32 scans from 4000 to 500 cm^{-1}. Contact angle results were obtained from a DataPhysics OCA30 instrument. An optical microscope equipped with CCD and a monochromator was used for the in situ optical observations.

Density functional theory (DFT) calculations

The optimized structures and the binding energies were calculated at the DFT level as implemented in the Vienna Ab initio Simulation Package (VASP), using a planewave basis set with an energy cutoff of 500 eV, the projector augmented wave (PAW) potentials, and the generalized gradient approximation (GGA) parametrized by Perdew-Burke-Ernzerhof (PBE) for the exchange and correction interactions. The Brillouin zone was sampled by $2\pi \times 0.04$ A^{-1} k-points using the Monkhorst-Pack scheme for $4 \times 4 \times 2$ supercells. The convergence criterions of energy and force calculations were set to 1×10^{-5} eV and 0.01 eV Å^{-1}, respectively. A vacuum region of 20 Å was applied to avoid interactions between the neighboring configurations. Binding energy (ΔE_b) was calculated as follows: $\Delta E_b = E_{tot} - E_{sub} - E_{Zn}$, where E_{tot} is the total energy of Zn-binding models, E_{sub} is the energy of each substrate, and E_{Zn} is the energy per Zn atom in the bulk Zn metal.

Finite element analysis (FEA) simulations

The COMSOL Multiphysics software was used to simulate the local current density, Zn^{2+} ion flux and deposition sites of various 3D hosts during plating process. Before the simulation, a half-cell electrodeposition system of 40 × 45 μm was constructed and the geometric models of bare CP, *g*-PSiO_x-NH_2/CP, *g*'-Ag/CP, and *g*'-Ag/*g*-PSiO_x-NH_2/CP were designed. Here, a single carbon fiber in the CP was represented by a rectangle of 0.5 × 30 μm. The ionic conductivity of 2.0 M $ZnSO_4$ aqueous electrolyte was set to be about 5.0 S m^{-1}, and the current density was set to 1.0 mA cm^{-2}. The relation between the diffusion coefficient and electric mobility follows the Nernst-Einstein relation. The Zn^{2+} transfers by the concentration diffusion in model follow the Fick's law. The local current density is calculated according to the Butler-Volmer Eq. 1

$$i_{loc} = i_0\left[\exp\left(\frac{\alpha_a F\eta}{RT}\right) - \exp\left(\frac{-\alpha_c F\eta}{RT}\right)\right] \quad (1)$$

where i_{loc} represents the current density of the electrode, i_0 is the exchange current density, α_a is the charge transfer coefficient in the anode direction, F represents the Faraday constant, η represents the activation overpotential, R represents the ideal gas constant, T represents the temperature in Kelvin, and α_c represents the charge transfer coefficient in the cathode direction. The ion migration behavior is studied according to the diffusion and electric field migration Eq. 2

$$N_{Zn} = -D_{Zn}\nabla c_{Zn} - Z_{Zn}\mu_{m,Zn}Fc_{Zn}\nabla\phi_l \quad (2)$$

where N_{Zn} is the Zn^{2+} diffusion flux, D_{Zn} is the Zn^{2+} diffusion coefficient, ∇c_{Zn} is the Zn^{2+} concentration gradient, $\mu_{m,Zn}$, represents mobility of Zn^{2+}, Z_{Zn} represents the Zn^{2+} band charge, and ϕ_l represents the electric potential in solution.

Fabrication of the batteries and electrochemical measurements

For the assembly of asymmetric Zn||Zn batteries, these 3D hosts (such as CP, *g*-PSiO_x-NH_2/CP, *g*'-Ag/CP, and *g*'-Ag/*g*-PSiO_x-NH_2/CP) were used as the working electrodes, a piece of zinc foil was used as the counter electrode, glass fiber membrane as the separator and 2.0 M $ZnSO_4$ as the electrolyte. CR2032-type coin cells were assembled to evaluate the reversibility and coulombic efficiency (CE) during the long-term Zn plating/stripping process. For the assembly of symmetrical Zn||Zn batteries, a certain amount of Zn was pre-deposited on these 3D hosts as working and counter electrodes (such as Zn/CP, Zn/*g*-PSiO_x-NH_2/CP, Zn/*g*'-Ag/CP, and Zn/*g*'-Ag/*g*-PSiO_x-NH_2/CP). Using the same electrolyte as above, CR2032-type coin cells were assembled to assess the long-cycling stability and rate performance at different current densities and capacities.

To evaluate their practical applicability, Zn||MnO_2 full batteries were assembled with a multi-component gradient confined Zn anode (such as Zn/CP, Zn/*g*-PSiO_x-NH_2/CP, Zn/*g*'-Ag/CP, and Zn/*g*'-Ag/*g*-PSiO_x-NH_2/CP), a MnO_2/CP cathode (MnO_2 loading: ~1.2 mg cm^{-2}), a glass fiber separator and 70 μl (2.0 M $ZnSO_4$ + 0.2 M $MnSO_4$) aqueous electrolyte. Furthermore, large-size pouch-type batteries (6 × 7 cm^2) were fabricated to demonstrate scalability, using Zn/*g*'-Ag/*g*-PSiO_x-NH_2/CP anodes with pre-deposited Zn of 12 mAh cm^{-2}, and high-loading MnO_2/CF cathodes with a MnO_2 loading of 15 mg cm^{-2}, low negative/positive capacity ratio (N/P ≈ 2.6), and lean electrolyte (700 μl).

Additionally, the Tafel plots of Zn||Zn symmetric batteries were tested at a scan rate of 5.0 mV s^{-1} from −0.2 to 0.2 V. Electrochemical impedance spectroscopy (EIS) was performed using a CHI760e electrochemical workstation, with measurements taken across a frequency range from 100 kHz to 0.01 Hz at an alternating voltage amplitude of 10 mV. Cyclic voltammetry (CV) of Zn||MnO_2 full batteries was carried out at a scan rate of 0.5 mV s^{-1} between 0.8–1.8 V (vs. Zn/Zn^{2+}). All potentials are given versus Zn/Zn^{2+} and all electrochemical measurements were performed at 25°C. Moreover, the capacity retention (%) was calculated according to the following Eq. 3

$$\text{Capacity retention (\%)} = \frac{\text{Capacity}_x}{\text{Capacity}_0} \times 100\% \quad (3)$$

Where Capacity_x and Capacity_0 represent the specific capacity of a full battery at the *x*th cycle (e.g., the 1000th cycle) and the 2nd cycle, respectively.

Supplementary Materials

This PDF file includes:

Figs. S1 to S22
Tables S1 and S2

REFERENCES

1. P. Ruan, S. Liang, B. Lu, H. J. Fan, J. Zhou, Design strategies for high-energy-density aqueous zinc batteries. *Angew. Chem. Int. Ed. Engl.* **61**, e202200598 (2022).
2. C. Li, S. Jin, L. A. Archer, L. F. Nazar, Toward practical aqueous zinc-ion batteries for electrochemical energy storage. *Joule* **6**, 1733–1738 (2022).
3. J. Yang, B. Yin, Y. Sun, H. Pan, W. Sun, B. Jia, S. Zhang, T. Ma, Zinc Anode for Mild Aqueous Zinc-Ion Batteries: Challenges, Strategies, and Perspectives. *Nano Micro Lett.* **14**, 42 (2022).
4. H. Peng, Y. Fang, J. Wang, P. Ruan, Y. Tang, B. Lu, X. Cao, S. Liang, J. Zhou, Constructing fast-ion-conductive disordered interphase for high-performance zinc-ion and zinc-iodine batteries. *Matter* **5**, 4363–4378 (2022).
5. X. Guo, S. Zhang, H. Hong, S. Wang, J. Zhu, C. Zhi, Regulation methods for the Zn/electrolyte interphase and the effectiveness evaluation in aqueous Zn-ion batteries. *Energ. Environ. Sci.* **14**, 5669–5689 (2021).
6. X. Wang, X. Li, H. Fan, L. Ma, Solid electrolyte interface in Zn-based battery systems. *Nano Micro Lett.* **14**, 205 (2022).
7. D. Han, S. Wu, S. Zhang, Y. Deng, C. Cui, L. Zhang, Y. Long, H. Li, Y. Tao, Z. Weng, Q.-H. Yang, F. Kang, A corrosion-resistant and dendrite-free zinc metal anode in aqueous systems. *Small* **16**, 2001736 (2020).
8. Y. Feng, Y. Wang, L. Sun, K. Zhang, J. Liang, M. Zhu, Z. Tie, Z. Jin, Fluorinated interface engineering toward controllable zinc deposition and rapid cation migration of aqueous Zn-ion batteries. *Small* **19**, e2302650 (2023).
9. D. Xiong, L. Yang, Z. Cao, F. Li, W. Deng, J. Hu, H. Hou, G. Zou, X. Ji, In situ construction of high-density solid electrolyte interphase from MOFs for advanced Zn metal anodes. *Adv. Funct. Mater.* **33**, 2301530 (2023).
10. K. Wu, J. Yi, X. Liu, Y. Sun, J. Cui, Y. Xie, Y. Liu, Y. Xia, J. Zhang, Regulating Zn deposition via an artificial solid–electrolyte interface with aligned dipoles for long life Zn anode. *Nano Micro Lett.* **13**, 79 (2021).
11. M. Liu, W. Yuan, G. Ma, K. Qiu, X. Nie, Y. Liu, S. Shen, N. Zhang, In situ integration of a hydrophobic and fast-Zn^{2+}-conductive inorganic interphase to stabilize Zn metal anodes. *Angew. Chem. Int. Ed. Engl.* **62**, e202304444 (2023).
12. R. Zhao, Y. Yang, G. Liu, R. Zhu, J. Huang, Z. Chen, Z. Gao, X. Chen, L. Qie, Anti-corrosion elastic constraints: redirected Zn electrodeposition by an anti-corrosion elastic constraint for highly reversible Zn anodes. *Adv. Funct. Mater.* **31**, 2001867 (2021).
13. P. Chen, X. Yuan, Y. Xia, Y. Zhang, L. Fu, L. Liu, N. Yu, Q. Huang, B. Wang, X. Hu, Y. Wu, T. van Ree, An artificial polyacrylonitrile coating layer confining zinc dendrite growth for highly reversible aqueous zinc-based batteries. *Adv. Sci.* **8**, e2100309 (2021).
14. S. Jin, Y. Deng, P. Chen, S. Hong, R. Garcia-Mendez, A. Sharma, N. W. Utomo, Y. Shao, R. Yang, L. A. Archer, Solid-adsorbed polymer-electrolyte interphases for stabilizing metal anodes in aqueous Zn and non-aqueous Li batteries. *Angew. Chem. Int. Ed. Engl.* **62**, e202300823 (2023).
15. J. Yin, Y. Z. Wang, Y. P. Zhu, J. J. Jin, C. L. Chen, Y. Y. Yuan, Z. Bayhan, N. Salah, N. A. Alhebshi, W. L. Zhang, U. Schwingenschlögl, H. N. Alshareef, Regulating the redox reversibility of zinc anode toward stable aqueous zinc batteries. *Nano Energy* **99**, 107331 (2022).
16. G. Zhang, X. Zhang, H. Liu, J. Li, Y. Chen, H. Duan, 3D-printed multi-channel metal lattices enabling localized electric-field redistribution for dendrite-free aqueous Zn ion batteries. *Adv. Energy Mater.* **11**, 2003927 (2021).

17. L. Zeng, H. He, H. Chen, D. Luo, J. He, C. Zhang, 3D printing architecting reservoir-integrated anode for dendrite-free, safe, and durable Zn batteries. *Adv. Energy Mater.* **12**, 2103708 (2022).
18. J. Zhou, F. Wu, Y. Mei, Y. Hao, L. Li, M. Xie, R. Chen, Establishing thermal infusion method for stable zinc metal anodes in aqueous zinc-ion batteries. *Adv. Mater.* **34**, e2200782 (2022).
19. Y. Zeng, P. X. Sun, Z. Pei, Q. Jin, X. Zhang, L. Yu, X. W. Lou, Nitrogen-doped carbon fibers embedded with zincophilic Cu nanoboxes for stable Zn-metal anodes. *Adv. Mater.* **34**, e2200342 (2022).
20. S. Shi, D. Zhou, Y. Jiang, F. Cheng, J. Sun, Q. Guo, Y. Luo, Y. Chen, W. Liu, Lightweight Zn-philic 3D-Cu scaffold for customizable zinc ion batteries. *Adv. Funct. Mater.* **34**, 2312664 (2024).
21. Y. Mu, Z. Li, B.-k. Wu, H. Huang, F. Wu, Y. Chu, L. Zou, M. Yang, J. He, L. Ye, M. Han, T. Zhao, L. Zeng, 3D hierarchical graphene matrices enable stable Zn anodes for aqueous Zn batteries. *Nat. Commun.* **14**, 4205 (2023).
22. W. Li, H. Yao, K. Yan, G. Zheng, Z. Liang, Y.-M. Chiang, Y. Cui, The synergetic effect of lithium polysulfide and lithium nitrate to prevent lithium dendrite growth. *Nat. Commun.* **6**, 7436 (2015).
23. J. Wu, Z. Ju, X. Zhang, A. C. Marschilok, K. J. Takeuchi, H. Wang, E. S. Takeuchi, G. Yu, Gradient design for high-energy and high-power batteries. *Adv. Mater.* **34**, e2202780 (2022).
24. X. Zhang, Z. Y. Hui, S. King, J. Wu, Z. Ju, K. J. Takeuchi, A. C. Marschilok, A. C. West, E. S. Takeuchi, L. Wang, G. Yu, Gradient architecture design in scalable porous battery electrodes. *Nano Lett.* **22**, 2521–2528 (2022).
25. J. Yun, B.-K. Park, E.-S. Won, S. H. Choi, H. C. Kang, J. H. Kim, M.-S. Park, J.-W. Lee, Bottom-up lithium growth triggered by interfacial activity gradient on porous framework for lithium-metal anode. *ACS Energy Lett.* **5**, 3108–3114 (2020).
26. Z. X. Shen, L. Luo, C. W. Li, J. Pu, J. P. Xie, L. T. Wang, Z. Huai, Z. Y. Dai, Y. G. Yao, G. Hong, Stratified zinc-binding strategy toward prolonged cycling and flexibility of aqueous fibrous zinc metal batteries. *Adv. Energy Mater.* **11**, 2100214 (2021).
27. L.-L. Lu, Y.-Y. Lu, Z.-X. Zhu, J.-X. Shao, H.-B. Yao, S. Wang, T.-W. Zhang, Y. Ni, X.-X. Wang, S.-H. Yu, Extremely fast-charging lithium ion battery enabled by dual-gradient structure design. *Sci. Adv.* **8**, eabm6624 (2022).
28. J. Pu, J. Li, K. Zhang, T. Zhang, C. Li, H. Ma, J. Zhu, P. V. Braun, J. Lu, H. Zhang, Conductivity and lithiophilicity gradients guide lithium deposition to mitigate short circuits. *Nat. Commun.* **10**, 1896 (2019).
29. J. Dong, H. Peng, J. Wang, C. Wang, D. Wang, N. Wang, W. Fa, X. Jiang, J. Yang, Y. Qian, Molecular deciphering of hydrophobic, zinc-philic and robust amino-functionalized polysilane for dendrite-free Zn anode. *Energy Storage Mater.* **54**, 875–884 (2023).
30. Y. Wang, Z. Wang, L. Zhao, Q. Fan, X. Zeng, S. Liu, W. K. Pang, Y.-B. He, Z. Guo, Lithium metal electrode with increased air stability and robust solid electrolyte interphase realized by silane coupling agent modification. *Adv. Mater.* **33**, e2008133 (2021).
31. E. M. Marti, C. Methivier, C. M. Pradier, (S)-Cysteine Chemisorption on Cu (110), from the gas or liquid phase: an FT-RAIRS and XPS study. *Langmuir* **20**, 10223–10230 (2004).
32. R. Zhang, X. Chen, X. Shen, X.-Q. Zhang, X.-R. Chen, X.-B. Cheng, C. Yan, C.-Z. Zhao, Q. Zhang, Coralloid carbon fiber-based composite lithium anode for robust lithium metal batteries. *Joule* **2**, 764–777 (2018).
33. Z. Du, H. Lu, D. Zhang, Z. Li, X. Yuan, M. Song, W. Zhang, X. Jiang, Y. Jin, Scalable fabrication and cost-effective graphite-paper-based zinc anode for promoting reversible cycling of zinc (002) crystallographic plane. *Energy Environ. Mater.* **9**, e70146 (2025).
34. H. Yu, Y. Zeng, N. Li, D. Luan, L. Yu, X. Lou, Confining Sn nanoparticles in interconnected N-doped hollow carbon spheres as hierarchical zincophilic fibers for dendrite-free Zn metal anodes. *Sci. Adv.* **8**, eabm5766 (2022).
35. Q. Li, H. Wang, H. Yu, M. Fu, W. Liu, Q. Zhao, S. Huang, L. Zhou, W. Wei, X. Ji, Y. Chen, L. Chen, Engineering an ultrathin and hydrophobic composite zinc anode with 24 μm thickness for high-performance Zn batteries. *Adv. Funct. Mater.* **33**, 2303466 (2023).
36. H. Y. Qin, W. Kuang, D. Huang, X. Y. Zhang, J. Liu, L. Yi, F. Shen, Z. Wei, Y. P. Huang, J. Xu, H. B. He, Achieving high-rate and high-capacity Zn metal anodes via a three-in-one carbon protective layer. *J. Mater. Chem. A* **10**, 17440–17451 (2022).
37. Y. Li, H. Jia, U. Ali, H. Wang, B. Liu, L. Li, L. Zhang, C. Wang, Successive gradient internal electric field strategy toward dendrite-free zinc metal anode. *Adv. Energy Mater.* **13**, 2301643 (2023).
38. P. X. Sun, Y. Q. Zheng, X. Y. Zhang, H. Yu, Y. Guo, L. Yu, Spatial confinement of Sn/TiO_2 nanoparticles in hollow mesoporous carbon spheres opal for stable Zn metal anodes. *Adv. Energy Mater.* **14**, 2304138 (2024).
39. J.-H. Wang, L.-F. Chen, W.-X. Dong, K. Zhang, Y.-F. Qu, J.-W. Qian, S.-H. Yu, Three-dimensional zinc-seeded carbon nanofiber architectures as lightweight and flexible hosts for a highly reversible zinc metal anode. *ACS Nano* **17**, 19087–19097 (2023).
40. X. Li, M. Li, K. Luo, Y. Hou, P. Li, Q. Yang, Z. Huang, G. Liang, Z. Chen, S. Du, Q. Huang, C. Zhi, Lattice matching and halogen regulation for synergistically induced uniform zinc electrodeposition by halogenated Ti_3C_2 MXenes. *ACS Nano* **16**, 813–822 (2022).
41. G. Chen, Z. Sang, J. Cheng, S. Tan, Z. Yi, X. Zhang, W. Si, Y. Yin, J. Liang, F. Hou, Reversible and homogenous zinc deposition enabled by in situ grown Cu particles on expanded graphite for dendrite-free and flexible zinc metal anodes. *Energy Storage Mater.* **50**, 589–597 (2022).
42. H. Wang, Y. Chen, H. Yu, W. Liu, G. Kuang, L. Mei, Z. Wu, W. Wei, X. Ji, B. Qu, L. Chen, A multifunctional artificial interphase with fluorine-doped amorphous carbon layer for ultra-stable Zn anode. *Adv. Funct. Mater.* **32**, 2205600 (2022).
43. Y. Gao, Q. Cao, J. Pu, X. Zhao, G. Fu, J. Chen, Y. Wang, C. Guan, Stable Zn anodes with triple gradients. *Adv. Mater.* **35**, e2207573 (2023).
44. Z. Zhang, Y. Kang, Z. Shan, Q. Zhang, Y. Wang, J. Yang, Y. Li, Y. He, Y. Geng, G. Chang, S. Ramakrishna, Seeram Ramakrishna, Nickel-doped zinc oxide as a zincophilic three-dimensional host for aqueous zinc batteries. *Chem. Eng. J.* **530**, 173142 (2026).
45. Y. Zeng, Z. Pei, D. Luan, X. W. Lou, Atomically dispersed zincophilic sites in N, P-co-doped carbon macro-porous fibers enable efficient Zn metal anodes. *J. Am. Chem. Soc.* **145**, 12333–12341 (2023).

Acknowledgments

Funding: This work was supported by the National Natural Science Foundation of China (U25A20628, 22561160129, 22479074, 22475096), the Equipment Pre-Research and Ministry of Education Joint Fund (8091B02052407), the Fundamental Research Program Key Project of Jiangsu Province (BK20253008), the Science and Technology Major Project of Jiangsu Province (BG2024013), the Scientific and Technological Achievements Transformation Special Fund of Jiangsu Province (BA2023037), the Academic Degree and Postgraduate Education Reforming Project of Jiangsu Province (JGKT24_C001), the Key Core Technology Open Competition Project of Suzhou City (SYG2024122), the Open Research Fund of Suzhou Laboratory (SZLAB-1308-2024-TS005), the Chenzhou National Sustainable Development Agenda Innovation Demonstration Zone Provincial Special Project (2023sfq11, 2025sfq38), and the Fundamental Research Funds for the Central Universities and Nanjing University International Collaboration Initiative (020514380354). **Author contributions:** Conceptualization: Z.J. and J.S. Methodology: Z.J. and J.S. Validation: Z.J., J.S., T.S., M.Z., Y.X., and J.W. Formal analysis: J.S., T.S., and M.Z. Investigation: J.S., T.S., Y.X., J.W., and Q.Y. Resources: Z.J., J.S., T.S., M.Z., Y.X., J.W., Q.Y., and Z.T. Data curation: J.S. Visualization: Z.J., J.S., T.S., and M.Z. Supervision: Z.J. Writing—original draft: Z.J. and J.S. Writing—review and editing: Z.J., J.S., and T.S. Project administration: Z.J. Funding acquisition: Z.J. **Competing interests:** The authors declare no competing interests. **Data, code, and materials availability:** All data and code needed to evaluate and reproduce the results in the paper are present in the paper and/or the Supplementary Materials. Information on new materials is available in Materials and Methods.

Submitted 24 March 2026
Accepted 1 July 2026
Published 5 August 2026
10.1126/sciadv.aeh4699

ScienceAdvances

Multi-component gradients in 3D host frameworks enabled stack-type zinc plating/stripping for highly durable aqueous Zn-ion batteries

Jingjie Sun, Tianyu Shen, Mingyue Zhang, Yizhi Xing, Jie Wei, Qianchuan Yu, Zuoxiu Tie, and Zhong Jin

Sci. Adv. **12** (32), eaeh4699. DOI: 10.1126/sciadv.aeh4699

Science Advances (ISSN 2375-2548) is published by the American Association for the Advancement of Science. 1200 New York Avenue NW, Washington, DC 20005. The title *Science Advances* is a registered trademark of AAAS.